nature portfolio

https://doi.org/10.1038/s41586-022-04770-6

Supplementary information

Fossil biomolecules reveal an avian metabolism in the ancestral dinosaur

In the format provided by the authors and unedited

Supplementary Information

Fossil biomolecules reveal an avian metabolism in the ancestral dinosaur

Jasmina Wiemann[1]*, Iris Menéndez[2,3], Jason M. Crawford[4], Matteo Fabbri[1], Jacques A. Gauthier[1,5], Pincelli M. Hull[1,5], Mark A. Norell[6], and Derek E. G. Briggs[1,5]

Supplementary Information includes:

1. Specimen selection

Modern, adult specimens (n=25 femora, n=10 ulnae, metatarsals, skull bones, ribs, vertebrae) were selected from the Yale Peabody Museum Division of Vertebrate Zoology (Supplementary Data 1 tab 2) for maximum phylogenetic coverage. Fossil specimens (n=13 eggshells, n=8 teeth, n=30 long bones including 28 femora, 1 humerus, a cetacean, and 1 vertebra, a snake) were selected for macroscopic evidence of 'carbonaceous' residues and phylogenetic diversity. Specimens with preserved organic matter were identified on the basis of previously published criteria[1]. We focused primarily on fossils that show a dark brownish or black discolouration which stands out against a light-coloured sediment matrix. Light-coloured sediments are usually low in sedimentary organic matter which could potentially 'contaminate' endogenous, fossil organic matter. Most fluvial, alluvial, aeolian, and shallow marine sediments fostered early diagenetic oxidative crosslinking as a prerequisite to biomolecule fossilization[1,2]. We have augmented specimens known to preserve fossil organic matter based on analyses published in Wiemann et al. (2018a)[1]—fossil vertebrate teeth, bones, eggshells, Wiemann et al. (2018b)[3]— fossil vertebrate eggshells, and Wiemann et al. (2020)[2], with additional specimens from suitable depositional environments. Wiemann et al. (2020)[2] confirmed the presence and endogeneity of fossil organic matter for most samples used in this study (please compare specimen lists: Wiemann et al. 2020[2], Supplementary Data 'Specimen data'). Age data are available for all modern and fossil samples, but information on latitudes is incomplete, and there is no information on paleo-altitudinal preferences.

All specimen ages and catalog numbers are recorded in Supplementary Data 1 tabs 1, 2. Catalog numbers can be used to access more detailed specimen data and photographs (as available) in the online catalog of the Yale Peabody Museum of Natural History Collections.

2. Method details

a. Methods summary

Fossil hard tissues (n=51), sediments (n=15) and modern skeletal elements (n=35) were surface-cleaned and subjected to *in situ* Raman microspectroscopy (532 nm, 500-1800 cm^{-1}, 10s, 10 replicates), and a subset (n=4) to *in situ* ATR FT-IR spectroscopy (632 nm, 500-3000 cm^{-1}, 32 replicates). Spectra were processed and analyzed in SpectraGryph 1.2 (Supplementary Information Sections 2a, b). Relative intensities at 24 band positions were selected to determine the endogenous nature and completeness of the metabolic signal in fossils: fossil-sediment,

fossil eggshell-tooth-bone, and fossil femora data sets were subjected to ordination methods (Supplementary Information Sections 2d, 3). Signal intensities from metabolic markers at 670, 1585, and 1685 cm^{-1} were extracted for fossil and modern femora, and crosslink-to-peptide signal ratios ($MC_{in\ vivo}$) calculated (Supplementary Information Section 2e). $MC_{in\ vivo}$ values of modern femora were regressed (PAST 3.0) against published metabolic rates and the fit was used for converting values into metabolic rates. Intraskeletal variation of signals was characterized for *Chironectes* and *Iguana*. A linear regression (PAST 3.0) for femora of fossils with extant relatives (n=8) (Supplementary Data 1 tab 3) determined a function that converts fossil $MC_{in\ vivo}$ values into metabolic rates. Mass specific metabolic rates were calculated for all fossil and modern long bones and plotted (log-log) against published body masses: A 95%-confidence interval was based on known endotherms in this sample. Variation in metabolism was assessed for non-avian ornithodirans, crown mammals, birds, and lepidosaurs. Metabolic rates were superimposed on a time-scaled phylogenetic framework (R) and ancestral states were reconstructed (Supplementary Information Section g-h).

b. *In situ* Raman microspectroscopy

Modern and fossil specimens were analyzed separately. All samples were surface-cleaned with 70% ethanol and immediately subjected to high resolution *in situ* Raman microspectroscopy in the Department of Earth and Planetary Sciences (formerly Geology and Geophysics) at Yale University. Raman microspectroscopy was performed using a Horiba LabRam HR800 with 532 nm excitation (20 mW at the sample surface; regularly replaced holographic notch filter). No heat damage was observed for the analyzed samples. The spectra were obtained in LabSpec 5 software (spectra acquisition, standard spike removal). The scattered Raman light was detected by an electron multiplying charge-coupled device (EM-CCD) following dispersal with an 1800 grooves/mm grating and passed through a 200 μm slit (hole size 300 μm). The spectrometer was calibrated using the first order Si band at 520.7 cm^{-1}. Ten spectra were accumulated in the 500-1800 cm^{-1} region for 10s exposure each, at 32x magnification. Spectra for specimens shown in the Extended Data Fig. 4 were acquired in the 500-3000 cm^{-1} range. All spectra were analyzed in SpectraGryph 1.2[4] spectroscopic software (adaptive baseline, 30%, no offset, minimally smoothed through rectangular averaging over an interval of 4 points, normalization), and exported to main text Fig. 1a to qualitatively identify spectral regions of maximum variability in their signal intensity.

c. *In situ* Attenuated-Reflectance Fourier-Transform Infrared Spectroscopy

Allosaurus (fossil), *Furcifer* (modern), *Chironectes* (modern), and *Puma* (modern) femora were surface-cleaned with 70% ethanol and immediately subjected to Attenuated-Reflectance Fourier-Transform Infrared (ATR FT-IR) Spectroscopy using an Agilent Technologies Cary 660 Series FT-IR Spectrometer with a diamond crystal Pike GladiATR module at the Yale West Campus Analytical Core (WCAC). FT Mid-infrared spectroscopy was performed for n=32 technical replicates per sample using a 632 nm laser to characterize moleuclar signatures over the whole spectral range, from 500-3000 cm^{-1}. Prior to sampling a background spectrum was taken and automatically subtracted by the Agilent Resolutions Pro Software. The diamond crystal and sampling area were carefully cleaned with isopropyl alcohol between each sample run. All collected spectra were normalized in SpectraGryph 1.2[4] spectroscopic software.

Fourier-Transform Infrared Spectroscopy targets a different type of interactions between chemical bonds and light when compared to Raman spectroscopy, and is by design not affected by sample fluorescence or other filter artefacts occasionally observed for Raman spectra. Negative peaks or bands in FT-IR spectra characterize based on their x-axis shift (wavenumber) different molecular functional groups, organo-mineral interactions, and crystal lattice vibrations, and produce data complementary to Raman spectra. Cross-validation of S-crosslinks, here identified as carrier of metabolic information in deep time, with Raman and FT-IR spectroscopy yields unambiguous bands assignments.

The ATR FT-IR net enrichment plot shown in the Extended Data Fig. 6 is the result of a subtraction of averaged modern bone spectra (n=3) from fossil bone spectra (n=1), performed in SpectraGryph 1.2[4].

d. Raman band selections and ChemoSpace Analyses

Relative intensities were selected at 24 informative band positions (Supplementary Data 1 tab 12) to determine which type of fossil hard tissues (eggshells, teeth, bones) is most suitable for metabolic assessments. As suggested by Wiemann et al. (2020)[2], bone tissues might record the most complete metabolic signals. The Raman 24 band positions were selected based on peak prominence after spectral superimposition in SpectraGryph 1.2 and compositional insights published in Wiemann et al. (2020)[2]. This band set represents key features of the total organic composition. All 24 bands are identified in the Supplementary Data 1 tab 12: 511, 529, 575, 629, 661, 777, 841, 878, 913, 1009, 1033, 1182, 1230, 1278, 1350, 1408, 1453, 1489, 1554,

1576, 1587, 1684, 1704, 1777 cm^{-1} Raman shift. Corresponding band assignments for the signals within the analyzed organic fingerprint region can be found in Wiemann et al. (2020)[2], additional Raman (and FT-IR) signals beyond the organic fingerprint region (not analyzed here) can be found in the Supplementary Data 1 tab 15. Relative signal intensities were selected at these band positions for normalized spectra of all fossil bones, teeth and eggshells, and the resulting taxon character matrix can be found in Supplementary Data 1 tab 12. The complete taxon-character matrix was subjected to a ChemoSpace Principal Component Analysis (PCA) in PAST 3[5], while a subsample of femora was also subjected to a separate Discriminant analysis.

The ChemoSpace PCA (Extended Data Fig. 1a) included n=51 fossil samples, and the key biological signals found along PC 1 and 2 were characterized based on PC loadings and insights from Wiemann et al. (2020)[2]. The PCA biplot is shown (Extended Data Fig. 1a), illustrating how different N- and S-heterocycles, common metabolic crosslinks[6], impact the biological signals along PC 1 and 2. Generally, avascular and acellular tissues (eggshells) separate from vascular and cellular tissues (bones and teeth), as highlighted by the convex hulls.

The separate Discriminant Analysis of fossil femora (Extended Data Fig. 1b) includes a subset of n=30 samples (identified in Supplementary Data 1 tab 12). Fossil taxa with published inferences of their thermal strategy were coded as ectothermic = 0, or endothermic = 1. Fossil taxa without published thermal inferences (see Supplementary Tab. 1 for thermal strategy assignments) were coded based on analyses in this study (Supplementary Information Sections 2d-g). The discriminant factors are presented in a biplot, and eigenvectors are identified as N- and S-crosslinks representative of metabolic markers (Extended Data Fig. 1b). Interrogating molecular compositional data of fossil amniote bones revealed increased amounts of N- and S-metabolic crosslinks as a characteristic feature of taxa with elevated metabolic rates and corresponding endothermic strategy. Comparison of the vector length for N- and S-metabolic crosslinks unveiled S-crosslinks, characteristic reaction products of lipoxidation rather than glycoxidation processes[4], as the major signal contributor. Lipoxidation is known to be linked to metabolic stress and aerobic respiration pathways[6,7,8,9]. Since fossil bone appears to be the most suitable tissue to preserve metabolic markers, modern amniote bones were analyzed using *in situ* Raman microscopy to ground-truth the presence of such a metabolic signal (Supplementary Information Section 2b, Supplementary Data 1 tab 2).

To assess intraskeletal variability of potential metabolic signals, femora, ulnae, metatarsals, ribs, vertebrae and skull bones of the modern endotherm *Chironectes* and the ectotherm *Iguana* were analysed using the same in situ Raman spectroscopic protocol, and their

metabolic signatures ($MC_{in\ vivo}$ values, see below) were compared (Extended Data Fig. 2). Different skeletal elements record metabolic signals to a different extent, and intraskeletal variability of metabolic signals is more pronounced in the endotherm *Chironectes* than in the ectotherm *Iguana*. This suggests that analyses of metabolic rates should be focused on homologous skeletal elements to achieve maximum comparability of the metabolic signals extracted. We focused our analysis on femora in modern and fossil taxa (only one humerus fragment was used, for the fossil cetacean, and one vertebra, for a fossil snake).

e. Calculating metabolic rates

Since N- and S- metabolic crosslinks appear to be prime contributors to the metabolic signal preserved in fossil (Extended Data Fig. 1b) and modern skeletal tissues (plots in Supplementary Data 1 tab 5), relative intensities were selected for normalized spectra of fossil and modern amniote bones at the band positions 666 cm^{-1} (S-crosslinks = thioethers, mostly Advanced lipoxidation end products [ALEs]), 1580 cm^{-1} (N-crosslinks = N-heterocycles, ALEs and Advanced glycoxidation end products [AGEs]), and 1683 cm^{-1} (peptide bonds = *trans*-amides) Raman shift.

For modern skeletal tissues, the calculated ratio of S- and N-crosslinks per peptide bond directly reflects the degree of metabolic oxidation: all calculated $MC_{in\ vivo}$ values can be found in Supplementary Data 'Extant Taxa'. The empirical $MC_{in\ vivo}$ (= Metabolic Crosslinks *in vivo*) value scales with the relative abundance of *in vivo* formed N- and S-crosslinks representing primarily oxidative metabolic stress:

$$\mathbf{MC}_{\boldsymbol{in\ vivo}} = \frac{([\mathrm{S-crosslinks}] + [\mathrm{N-crosslinks}])}{[trans-\mathrm{amides}]}$$

For these modern taxa, published metabolic rates were compiled[10-21], and a linear regression was fitted (standard least squares; in PAST 3) for $MC_{in\ vivo}$ values and published metabolic rates. Published metabolic rates, as well as all details of the linear regression, can be found in the Supplementary Data 'Extant Taxa'. Based on the regression (published metabolic rates *versus* spectral $MC_{in\ vivo}$ values) spectral metabolic rates were calculated for all extant taxa using the following equation (Extended Data Fig. 4):

$$f(x) = 9.5273 \times MC_{in\ vivo} - 8.0604$$

The regression was performed in PAST 3, and a Kernel plot (main text Fig. 1e) was exported to assess the accuracy of spectral metabolic rate data beyond p (5.62×10^{-7}), Pearson's r (0.82), r^2 (0.67), and Spearman ranks correlation (0.74). Raman-based metabolic rate assessments are significantly representative of reported metabolic rate data. The kernel plot (Fig. 1e) reveals that, compared to published metabolic rate data, spectrally inferred metabolic rates tend to slightly underestimate rather than overestimate metabolic rates. To avoid negative values for metabolic rates calculated from spectral data, all resulting values for modern taxa (only femora) were corrected by adding +1.2 (Fig. 1e; Supplementary Data 1 tab 2). For fossil taxa, a correction by +0.4 would avoid negative values, however, considering that the data set consists of 28 femora, 1 humerus, and 1 vertebra, the maximum uncertainty related to intraskeletal variation (+0.9) was added, as recovered in Extended Data Fig. 2 (Fig. 1e; Supplementary Data 1 tab 2).

To ensure maximum comparability of the metabolic signals extracted, samples were analysed consecutively, ideally in one run. Samples that were added during the revision of this manuscript had to be collected with a different Raman objective (20x), and the resulting changes in the geometry of the light path required scaling (+ 0.3) to match the original data set. Affected taxa are highlighted in the Supplementary Data 1 (tab 2).

Fossil skeletal tissues pose an additional challenge, as they contain not only metabolic crosslinks, like their modern tissue analogues, but also diagenetically induced crosslinks. The calculated $MC_{in\ vivo}$ value allows for the consideration of diagenetic crosslinks. Fossilization generates N- and S-heterocycles from advanced lipoxidation and glycoxidation processes involving originally proteinaceous matter and reactive carbonyl species (RCS) formed from lipids or sugars. Diagenetic transformations were considered by calculating a ratio from the relative signal intensities of N- and S-heterocycles and the relative signal intensity of preserved, unaltered peptide bonds. In contrast to metabolic crosslinking, diagenetic crosslinking more commonly transforms peptide bonds (=*trans*-amides)[1,2,6] – thus the relative abundance of peptide bonds, as encoded in the normalized *trans*-amide signal intensity, offers a measure of the extent of diagenetically induced crosslinking. Understanding the degree of advanced crosslinking is important, as S- and N-crosslinks in fossil skeletal tissues are formed in part *in vivo* via oxidative metabolic stress, and in part diagenetically. Just as in their modern bone analogues, $MC_{in\ vivo}$ values were calculated for fossils.

A separate calibration was required to understand how fossil $MC_{in\ vivo}$ values scale with corresponding metabolic rates. To establish this scaling relationship, fossil taxa with living relatives were selected (n=8). Published metabolic[10-21] rates were compiled for these taxa

represented by both fossil and modern samples (Supplementary Data 1 tab 3, main text Fig. 1b), covering multiple taxa of the clades Aves, Mammalia, and Lepidosauria. A linear regression was performed in PAST 3 (literature metabolic rates for extant relatives *versus* fossil $MC_{in\ vivo}$ values). Details of the regression function can be found in Supplementary Data 1 tab 3. Based on the linear regression, fossil metabolic rates were calculated using the following equation:

$$f(x) = 1.2994 \times MC_{in\ vivo} - 3.9047$$

For fossil taxa, a correction of the calculated values by +0.4 would avoid negative values, however, considering that the data set consists of 28 femora, 1 humerus, and 1 vertebra, the maximum uncertainty related to intraskeletal variation (+0.9) was added, as recovered in Extended Data Fig. 2 (Fig. 1e; Supplementary Data 1 tab 2).

Resulting metabolic rates are listed in Supplementary Data 'Fossil Taxa'. All statistical analyses were performed in PAST 3, and simple mathematical operations were performed in Microsoft Excel 2016. The Supplementary Data 1 spreadsheet includes all active functions, and lists data according to the workflow described here (i.e., tabs 1, 2). The separate calibration of fossils based on extant taxa allows for a true integration of fossil and modern amniote molecular metabolic data (Fig. 1d).

f. Log-log plot of metabolic rates for fossil and modern taxa

Corrected metabolic rate values for extant and fossil skeletal tissues are listed in Supplementary Data 1 tab 5, and published/catalogued body masses (for extant taxa) and body mass estimates (for fossil taxa)[22-26] were added for each taxon. Since the extant and fossil calibrations produced metabolic rates corresponding in dimensions to milliliters oxygen respired per hour and per gram body weight (mL $O_2 \times h^{-1} \times g^{-1}$), all values were scaled for each taxon based on the body mass information, and both mass-specific metabolic rates and body masses were log-transformed in Microsoft Excel. All data and operations associated with the body mass-scaling and log-transformation are listed in Supplementary Data 'Modern & Fossil MRs'. Log mass-specific metabolic rate values were plotted against log body mass values in PAST 3 for all extant and fossil taxa, and a linear regression was fitted. The resulting plot is shown in the Supplementary Data and identifies all data points, in contrast to main text Fig. 1d which labels only fossil taxa. An additional comparison of the traditional linear regression of all data points, and a phylogenetically corrected linear regression (R, based on tree used in Fig. 2) are provided in the Supplementary Data 1 tab 14.

g. 95% confidence interval for endothermy

To assess thermal strategies based on reconstructed metabolic rates of extinct animals, a well-constrained confidence interval is required. We sub-sampled log-log data (mass-specific metabolic rates and body masses) for known endotherms[27]: extant mammals and birds and extinct crown mammals and birds (see Supplementary Information Section 2f for the calculation of log-log data; Supplementary Data 1 tab 6). The n=27 data points were separately plotted in PAST 3, and a 95% confidence interval was calculated (Supplementary Data 1 tab 6). The 95% confidence interval was calculated based on known endotherms, thus only 95% of all sampled, known endotherms fall within it. Endotherms plotting above the confidence interval exhibit higher metabolic rates. The only known endotherms that fall outside the confidence interval are crown mammals located right at the lower boundary of the endothermy CI (these taxa are identified in the Supplementary Data 1 tab 6). This plot (shown in the Supplementary Data 1 tab 6 fully labelled) was exported and superimposed on the log-log plot generated following the procedures explained in Supplementary Information Section 2g (main text Fig. 1d). All details for the calculated endothermy confidence interval can be found in Supplementary Data 1 tab 6.

Because this is a 95%-confidence interval, some endotherms plot right at the edge, while 5% of the endotherms used for the calibration of the confidence interval plot outside it. When assessing thermal strategies, we considered that the Raman approach tends to underestimate metabolic rates (Fig. 1e), and therefore considered fossils plotting at the lower margin of the endothermy confidence interval as endotherms, as well as any taxon plotting within and above the crown endothermy confidence interval. Mass-specific metabolic rates higher than those of known endotherms can only result in endothermy.

To make sure that the body mass scaling and logarithmic transformation of calculated metabolic rates do not introduce a signal that may not be present in the raw data, we also generated a scatter plot of unaltered $MC_{in\ vivo}$ values including those for all modern and fossil taxa (Extended Data Fig. 3, Supplementary Data 1 tab 5). Data points are coloured based on known thermal strategy (for extant and extinct crown mammals and birds), and fossils were coloured based on the published literature[20,28-33]. Where no data on thermal strategy were available, fossil assessments were based on the results for thermal strategies in fossils shown in Fig. 1d. Endotherms plot, even without any consideration of body mass scaling or logarithmic transformation, consistently above ectotherms, demonstrating that the data presented in main text Fig. 1d represent a genuine signal.

Supplementary Tab. 1: Thermal assignments and literature sources for fossil samples included in Extended Data Fig. 1b and Extended Data Fig. 3.

Taxon	Thermal strategy	Source
Anseriform bird	Endotherm	Avian
Diplodocid	Endotherm	Based on Fig. 1d, Legendre et al. 2016[20]
Rhamphorhynchoid	Endotherm	De Ricqles et al. 2000[28]
Hesperornis	Endotherm	Avian
Pachycephalosaur	Endotherm	Based on Fig. 1d, Legendre et al. 2016[20]
Allosaurus	Endotherm	Legendre et al. 2016[20]
Deinonychus	Endotherm	Rezende et al. 2020[29]
Brontothere	Endotherm	Mammalian
Nodosaurus	Endotherm	Based on Fig 1d
Telmatornis	Endotherm	Avian
Saniwa	(facult.) Endotherm	Christian & Conley 1994[30], Tattersall et al. 2016[31]
Marsupial	Endotherm	Mammalian
Insectivore	Endotherm	Mammalian
Cetacean	Endotherm	Mammalian
Tyrannosaurus	Endotherm	Rezende et al. 2020[29], Amiot et al. 2006[32]
Dryosaurus	Endotherm	Fig. 1d, Legendre et al. 2016[20]
Pteranodon	Endotherm	De Ricqles et al. 2000[28]
Polyglyphanodon	Ectotherm	Lepidosaur
Odaxosaurus	Ectotherm	Lepidosaur
Plesiosaur	Endotherm	Fleischle et al. 2018[33]
Melanosaurus	Ectotherm	Lepidosaur
Crocodylomorph	Ectotherm	Based on Fig. 1d, Legendre et al. 2016[20]
Hadrosaur	Ectotherm	Based on Fig. 1d, Legendre et al. 2016[20]
Xanthusiid	Ectotherm	Lepidosaur
Triceratops	Ectotherm	Based on Fig. 1d, Legendre et al. 2016[20]
Edaphosaurus	Ectotherm	Based on Fig. 1d
Stegosaurus	Ectotherm	Based on Fig. 1d, Legendre et al. 2016[20]
Champsosaur	Ectotherm	Based on Fig. 1d

Cteniogenys	Ectotherm	Based on Fig. 1d
Paleophis	Ectotherm	Lepidosaur

h. Ancestral state reconstruction of metabolic rates and thermal strategies

Corrected metabolic rate values (mL $O_2 \times h^{-1} \times g^{-1}$) as calculated in Supplementary Information Section 2e (and listed in Supplementary Data 1 tab 14) were compiled for all modern and fossil taxa included in this study and converted into continuous characters. Information on thermal strategies was added for each taxon, as inferred from the endothermy-confidence interval (main text Fig. 1d); thermal strategies were coded as ectothermy = 0, and endothermy = 1. The resulting taxon-character matrix was analyzed over an amniote consensus tree including all extant and fossil taxa analyzed in this study. The consensus tree is based on Upham et al. (2019)[34] for Mammalia, Simoes et al. (2018)[35] for the general relationships of the major groups composing Diapsida, Gauthier et al. (2012)[36] for the internal relationships of Squamata, Nesbitt et al. (2017)[37] for Archosauria and early dinosaurs, Brusatte et al. (2014)[38] for Theropoda and Prum et al. (2015)[39] for crown Aves. Ancestral character states were traced in Mesquite using a maximum parsimony algorithm. All original software outputs and codings are listed in Supplementary Data 1 tab 14. Analyses of alternative trees can also be found here.

Additionally, we applied a maximum likelihood reconstruction of continuous traits to the corrected metabolic rate values. To account for the possible effect of branch length on the ancestral reconstruction, we first time-scaled the consensus tree using *bin_timePaleoPhy* function on 'paleotree' package[40] in R language[41]. Terminal branches were scaled based on the stratigraphic ranges of each taxon[42], and certain nodes were constrained to a minimum age of divergence sampled from nodes' time intervals[43]. We used a minimum branch length of 1 Ma and obtained 1,000 time-scaled trees from which we calculated the consensus using the *consensus.edges* function in 'phytools' R package [44]. We inferred ancestral states using *fastAnc* function and plotted the results with *contMap* using 'phytools'[44].

The time-scaled analysis can be found in Fig. 2. All code and data for time-scaling the phylogenetic tree and for the maximum likelihood ancestral reconstruction is available at Github (https://github.com/IrisMenendez/Dinosaur_metabolism).

i. Correlation analyses

Corrected metabolic rates (mL $O_2 \times h^{-1} \times g^{-1}$) were compiled for all extant and fossil taxa (calculated following Supplementary Information Section 2e), and complemented with a

value representing the energy expense of the taxon's locomotion style, as well as the body mass (extant taxa) / body mass estimates (fossil taxa). The energy expense of locomotion styles were coded (inferred based on published data[45-49]) in the form of discrete characters ranging from a low energy expense to a high energy expense: quadrupedality = 0, bipedality = 1, flight/underwater flight = 2. Underwater flight is here defined as flipper-based underwater propulsion.

Individual correlation analyses were performed for these data in PAST 3, considering only extant taxa, only extinct taxa, or both. All values and details are listed in Supplementary Data 1 tab 9.

j. Assessing the impact of changes in atmospheric oxygen levels through time on animal metabolic rates

Fossil samples in the data set range in age from Permian to Tertiary, an interval of time that experienced fluctuations in atmospheric oxygen levels[50]. Considering that metabolic rate describes the amount of oxygen respired per unit time per unit body mass, the overall availability of atmospheric oxygen might impact not only the evolution of animal metabolic rates, but also the comparability of modern and fossil metabolic rates. However, the myriad of animal physicochemical adaptations to reduced or increased oxygen availability makes this difficult to test. We binned taxa by relative atmospheric oxygen levels into Permian samples (> 25% O_2)[50], Jurassic samples (~ 15% O_2)[50], Late Cretaceous/Tertiary samples (> 20% O_2)[50], and modern samples (~ 20% O_2)[50] and ran a correlation analysis of $MC_{in\ vivo}$ values (see Supplementary Data 'O_2 through time'). No correlation was found.

We further assessed the range of $MC_{in\ vivo}$ values realized for those taxon bins including multiple samples. While our data set contains only one Permian sample, n=8 Jurassic samples were grouped together, as well as n=21 Late Cretaceous and Tertiary samples, and n=25 modern samples. The metabolic ranges realized in each time bin are comparable, and reveal no fundamental differences.

Based on these insights, we infer that changes in atmospheric oxygen composition through time did not leave any detectable signature in the amniote metabolic rates obtained for this data set.

k. Overview of the analytical strategy

1. Spectral acquisition and standard processing (spike removal, baselining, smoothing, normalization) for fossil eggshells, bones, teeth, and sediments.

2. Selection of 24 bands that characterize the total organic composition (based on Wiemann et al. 2020) for all fossil eggshells, bones, teeth, and sediments.
3. Subjecting the fossil and sediment taxon-character matrix to a Non-linear Multidimensional Scaling Analysis (shown in Extended Data Fig. 1a – fossil tissues, and Supplementary Information Section 3).

   Result 1: Organic matter in the analysed samples is endogenous.
4. Assessing the biplot trajectories for bands encoding S- and N-crosslinks in fossil tissues which reveals that bone and dentine are characterized by increased amounts of ALEs (consistent with the results of Wiemann et al. 2020, Fig. 3b).
5. Noting that the analyses in Wiemann et al. 2020 (specifically Figs. 1a, 3b, 4b) show that the increased abundance of ALEs in bone corresponds to *in vivo* increased concentrations of ALEs which sort taxa in a ChemoSpace according to their presumed thermal strategy (Extended Data Fig. 1b, also in Wiemann et al. 2020), and therefore record metabolic information. Wiemann et al. (2020) explored biosignature fidelity in different tissue types, and showed that bone preserves a more accurate metabolic signal than dentine. Therefore, we chose bone as the target tissue for extracting metabolic information in ALEs in fossil and modern taxa.

   Result 2: ALEs in fossil bone appear to preserve metabolic information.
6. Spectral acquisition and standard processing for femora (identified as most suitable through assessments of intraskeletal variability of metabolic signals) of endothermic and ectothermic amniotes.
7. Calculating the crosslink-to-protein ratio ($MC_{in\ vivo}$) for all extant taxa and compiling metabolic rates for all analyzed taxa from the physiological publications.
8. Running a (linear) regression and assessing prediction performance with three distinct measures: Pearson's r, r^2, and Spearman ranks. There is a significant correlation between the abundance of ALEs (known markers of metabolic oxidative stress) and the metabolic rate in extant taxa. The resulting regression function is used as calibration function for extant taxa (yielding values equivalent to metabolic rates).

   Result 3: ALEs are present in modern bones in a relative abundance that reflects the metabolic rate. ALE crosslink-to-protein ratios can be transformed into metabolic rates using two different calibrations for fossil and extant bone.
9. Selecting fossils from the data set with close extant relatives which have published metabolic rates.

10. Calculating crosslink-to-protein ratios ($MC_{in\ vivo}$) for these selected fossils and performing a separate bivariate fit (=linear regression) against the published metabolic rates. Model performance shows a significant correlation between fossil crosslink-to-protein ratios (= $MC_{in\ vivo}$ values), and residuals are quantified to assess error margins (Supplementary Data). The resulting regression function is used to calibrate fossils.
11. Calculating crosslink-to-protein ratios ($MC_{in\ vivo}$ values) for all other fossils and applying the fossil calibration function (yielding values equivalent to metabolic rates).
12. Calculating mass-specific metabolic rates for modern and extinct crown mammal and birds and plotting them against corresponding body masses to generate the 95% confidence interval for endothermy.
13. Calculating mass specific metabolic rates for all other fossil taxa, plotting them against corresponding body masses, and projecting them onto the 95% confidence interval for endothermy.
14. Quantifying the uncertainty associated with Raman-based metabolic rates for extant taxa (shown in Fig. 1e), revealing that the Raman approach tends to slightly underestimate metabolic rates.
15. Assigning endothermy as the thermoregulatory strategy for fossils that plot at the lower boundary of, within, or above the endothermy confidence interval.
16. Downstream analyses of calculated metabolic rates (Ancestral State Reconstruction and correlation analyses).

Result 4: Figs. 1c-e, 2 and Supplementary Data 1 tab 9 provide insights into how metabolic rates evolved.

3. Organic matter endogeneity

Most of the fossil samples included in this study were previously analyzed by Wiemann et al. (2020)[2] to understand trends in the molecular composition of animal fossils. As part of the analytical framework presented in Wiemann et al. (2020)[2], a discriminant analysis distinguishing fossils and sediments was performed (Wiemann et al. 2020[2], Fig. 2d). All animal fossils analyzed showed little if any overlap in composition with sediment samples, suggesting an endogenous origin of biomolecular fossilization products. Key discriminating factors are abundant *trans*-amides (= peptide bonds), thioethers and S-heterocycles in endogenous fossil organic matter – all of these markers are abundant in the samples included in the present study. To incorporate the few specimens which were not included in the Wiemann et al. (2020)[2] data set, we performed a non-metric multidimensional scaling (NMDS) analysis (Supplementary

Fig. 1) of the 24 spectral bands selected for the ChemoSpace analysis (Extended Data Fig. 1). In addition, relative intensities were selected for all 24 Raman bands based on sediment spectra. These sediments represent fossil host rocks ranging in lithology from shales, to limestones, to sandstones (Supplementary Data 1 tab 13). The results of the NMDS are shown in Supplementary Figure 1, and reveal minimal compositional overlap between fossils and sediments. The compositional differences between fossils and sediments indicate endogeneity of fossil organic matter.

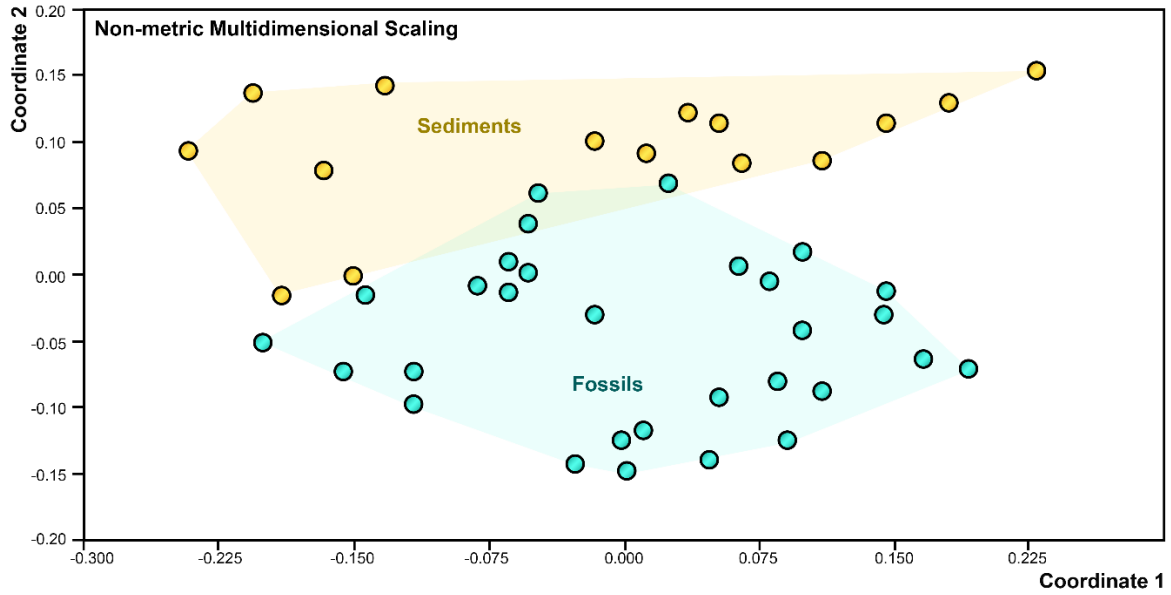

Supplementary Fig. 1: Non-metric multidimensional scaling of spectral data characterizing the composition of sediments (n=15) and the fossil bone samples they enclosed. Orange data points represent sediment samples (fossil host rocks ranging from black shales to sandstones); blue data points represent fossils. Accordingly, the orange convex hull contains all sediment samples and the blue convex hull contains all fossil specimens. Both clusters show minimal overlap, and are largely distinct in their molecular composition. All fossils and sediments samples are identified in Supplementary Data 'Fossils' and 'Sediments'.

4. Comparison of Raman metabolic rates and previous metabolic inferences

Previous attempts to understanding the evolution of amniote metabolic strategies were limited to indirect inferences based on histological quantification of growth and isotope fractionation-derived body temperature estimates. Fossilizable, molecular metabolic markers provide the first direct assessments of extinct amniote metabolism. This new molecular proxy will provide novel mechanistic insights into the evolution of amniote physiology,

complementary to our understanding of phenotypic and behavioural consequences, such as individual growth patterns and body temperatures.

a. Osteohistology

Osteohistology has proved to be a revolutionary tool for understanding the biology of extinct taxa: the study of bone tissue has yielded information on age[51-52], ecology[53], gender[54], reproductive traits[55], population dynamics[56-57], and development and its evolution[52,58-63]. Most non-avian dinosaurs show a cyclical, logistic growth[51]. 'Lines of Arrested Growth' (LAGs) and their zonation in the primary bone tissue are a prime target for inferences about individual growth rates throughout ontogeny. These insights can be scaled up into macroevolutionary hypotheses using taxonomically and systematically broad datasets. The maximum growth rate has long been the only proxy employed to estimate metabolic rates[52,58-64].

However, the translation of growth rates to metabolic rates is debated[20,60,64-66]. The quantification of maximum growth rates requires cyclical growth which results in LAGs in the bone tissues. Previous studies suggested that a minimum of five LAGs is required to fit a growth curve model[64-65] and therefore quantify growth rates. Preservation of a rather complete growth record is rare: the primary bone tissue is remodeled (through absorption and redeposition) during ontogeny, obscuring the early growth record[51]. A variety of approaches are available for retrocalculation of the remodeled (i.e., lost) LAGs[51] but the resulting maximum growth rate may vary substantially depending on the method used [51,53,58-63]. Alternatively, multiple individuals of the same taxon at different ontogenetic stages can be combined to fill gaps in the preserved growth record[51,58-63]. This approach suffers, however, from biases in the fossil record: not every taxon preserves multiple individuals.

Another topic of debate is the interpretation of the growth rate: growth fluctuates through the year[51-52,65-66]. Tetrapods show seasonal growth, with a maximum rate during specific periods and essentially no growth during the rest of the year[51-52,65-66]. Maximum growth rates are calculated as the highest yearly growth rate observed during ontogeny divided by the number of days per year. Therefore, the maximum growth rates of extinct taxa may be underestimated[65-66]. Underestimation of maximum growth rates leads to inaccuracies in growth rate-based inferences of metabolic rates and thermoregulatory strategies. Moreover, it is known that not all animals with high metabolic rates grow fast[60]: *Homo sapiens* shows high metabolism and is endothermic, but growth is relatively slow in comparison to other mammals[67]. An additional example of partial decoupling between thermoregulatory strategies and growth rates was revealed by this study: hadrosaurids show high growth rates[57,61] but we recovered low metabolic

rates in these animals compared to other dinosaurs. These results are in agreement with previous vascularization-based inferences of hadrosaurid metabolic rates[21]. Thus growth rates and metabolic rates are not necessarily coupled but both are fundamental to infer amniote physiology and its evolution. Their correlation for taxa included in this study (Supplementary Tab. 2) is visualized in Supplementary Fig. 2. A significant, moderately strong correlation is observed between histologically derived growth rates and spectrally calculated metabolic rates.

Additional histology-related approaches to determining metabolic rates in extinct animals target vascular diameters[20], and fossil blood cell structure and size[9], as a correlate of oxygen demand/oxygen availability per unit time. While there are promising case studies for both approaches, few comparative studies are available for these potential morphology-based proxies. Strengths and weaknesses of these various approaches are discussed in Supplementary Information Section 4d.

Supplementary Tab. 2: Log-transformed metabolic rates (main text Fig. 1d) and maximum growth rates (Gr max from Grady et al. 2015[64]).

Taxon	log MRs (mL $O_2 \times h^{-1} \times g^{-1}$)	Gr max ($g \times d^{-1}$)
Diplodocid	8.76	3.34
Allosaurus	7.31	2.49
Tyrannosaurus	7.53	3.11
Dendrocygna	3.89	1.08
Mustela	3.16	1.14
Varanus	3.5	0.67
Ara	3.67	1.45
Passer	2.17	0.59
Aotus	3.36	0.17
Ornithorhynchus	3.57	0.74
Tachyglossus	4.05	0.47
Agama	2.96	-0.41

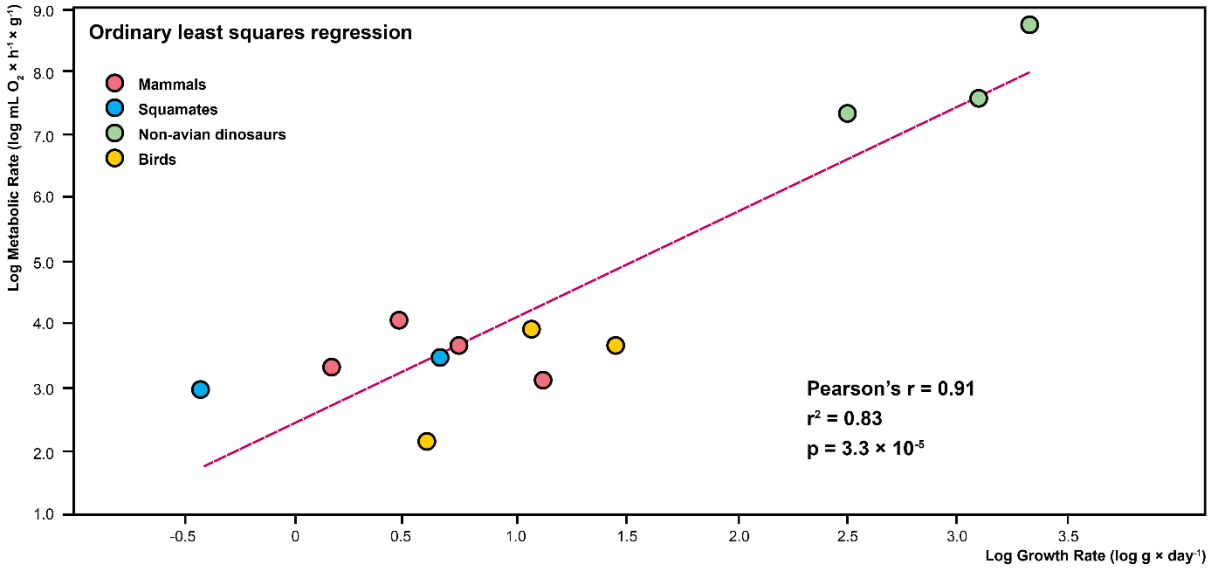

Supplementary Fig. 2: Ordinary least squares regression (linear regression) between metabolic rates (this study) and growth rates (from Grady et al. 2015[64]).

b. Isotopic inferences

Isotope fractionation has been used to infer body temperatures in extinct animals, such as marine reptiles[68] and dinosaurs[32,69-72]. Body temperature has been used to infer metabolism and thermoregulatory strategy. However, differences in palaeolatitude, diagenetic overprinting, and calibration of palaeothermometry add uncertainties to body temperature estimates. Body temperatures cannot distinguish between different thermal strategies, such as gigantothermy *versus* true endothermy *versus* behavioural thermoregulation. Our novel metabolic proxy therefore offers complementary insights to body temperatures estimated, as it distinguishes metabolic temperature regulation from behavioural temperature regulation.

c. Towards a multiproxy approach in paleophysiology

Molecular metabolic markers are direct proxies for aerobic respiration, and therefore metabolic rates, but cannot provide information on individual growth or absolute body temperatures. Our new proxy represents a complementary tool to infer physiology in extinct taxa. Indeed, as previous studies pointed out[60-66,67], growth rates, body temperature and metabolic rates are not necessarily tightly correlated. Advancing our understanding of physiological innovations in the history of amniotes is therefore dependent on the use of multiple proxies.

d. Strengths and weaknesses of different approaches to determining extinct animal metabolic rates and thermophysiology

Supplementary Tab. 3: Strengths and weaknesses of *in situ* Raman assessments.

Strengths	Weaknesses
***In situ* Raman microspectroscopy**	
Raman assessments of relative ALE abundances in fossil organic matter represent the only known, direct approach to extinct animal metabolic rates.	Each Raman microspectroscope requires individual calibration and potential minor adjustments of the exposure time, laser power, and number of accumulations based on the available instrumental set-up. Such adjustments have to be made before starting to analyze samples (as for other geochemical analytical routines).
The *in situ,* non-destructive approach safeguards unique fossils.	Raman intensity counts are arbitrary, and depend on the instrument calibration technique used. For ideal comparability, fossils (and sediments for assessments of organic matter endogeneity) should be analyzed in one run/shift or over consecutive days. Adding samples later on may require scaling to ensure comparability of spectral data.
When acquired over a large spectral range (i.e., 300 – 3000 cm^{-1}), Raman spectra reveal general patterns in the inorganic (=mineralogical), organic, and bio-inorganic (=organo-mineral) make-up of a sample.	The assessment of biological signatures in fossil organic matter with Raman spectroscopy is comparative in nature. Data can only be interpreted in the context of statistical analyses of comparable, large sample sets.
Raman allows rapid generation of informative data for large sample sets.	Raman spectroscopy of fossil organic matter has only been introduced to the paleontological community recently, so no large, collaborative databases are available yet.
Raman microspectroscopes are widely used in geology, material sciences, chemistry, biology/biomaterial sciences, clinical diagnostics.	The calibration for the empirical conversion of spectral data into metabolic rates is presently known only for amniotes. A deeper understanding of peculiarities in the lipoxidation biochemistry of non-amniotic vertebrates is required to establish suitable empirical calibrations for metabolic rate assessments in other taxa.
Technical replicates can easily be implemented in the analytical routine through an increased number of spectral accumulations.	

Raman spectral processing can be performed using freeware (i.e., SpectraGryph, etc.).	

Supplementary Tab. 4: Comparison of *in situ* Raman metabolic assessments with those of other techniques.

Extinct amniote metabolic rates and thermophysiological strategies	
Raman assessments of fossil organic matter	*Isotope geochemistry of hard tissue minerals*[33,68-72]
Raman assessments of the relative abundance of metabolic ALEs in modern and fossil amniote bones allow for the direct assessment of metabolic performance and resulting thermoregulatory strategies.	$\Delta^{18}O$ and clumped isotope ratio assessments provide insights into the temperature during mineral formation which, in the case of bones and eggshells, corresponds to body temperature. Generally, endothermic animals are capable of maintaining constant body temperatures, regardless of the environmental temperature, while the body temperature of ectotherms is known to co-vary with environmental temperatures. However, in warm climates, body temperatures of endo- and ectotherms differ only minimally. Therefore, inferences of thermoregulatory strategies based on body temperature reconstructions/body temperature fluctuations have to be treated with caution. Isotope geochemistry does not provide insights into extinct animal metabolic rates.
Diagenesis exacerbates differences in the original relative abundance of ALEs, making the separation of taxa with high versus low metabolic rates more pronounced and facilitating the direct inference of thermophysiological strategies.	Isotope ratios can be heavily affected by diagenesis, adding potential uncertainty to body temperature estimates.
Samples require only surface-cleaning with ethanol, and the analysis is non-destructive.	Requires destructive sampling and time-intensive preparation.
Samples can be analyzed without a standard, however, the empirical calibration of spectral $MC_{in\ vivo}$ values requires extant samples from taxa with known metabolic rates.	Samples require analysis against a standard.
Raman assessments of fossil organic matter	*Osteohistological assessments of growth rates*[29,34,53,65-67]
Raman assessments of the relative abundance of metabolic ALEs in modern and fossil amniote bones allow for the direct assessment of metabolic performance and resulting thermoregulatory strategies.	Growth rates are the result of metabolic performance, as is the thermoregulatory strategy. However, the incremental addition of body mass recorded in growth rates depends also on the availability of food

	sources and environmental factors (climate, precipitation, etc.). High growth rates are an indication of likely high metabolic rates resulting in endothermy, but both metabolic and thermophysiological inferences based only on growth rates are indirect.
Samples require only surface-cleaning with ethanol, and the analysis is fully non-destructive.	Requires destructive sampling and time-intensive preparation (sample cutting, embedding, polishing, etc.).
Diagenesis exacerbates differences in the original relative abundance of ALEs, making the separation of taxa with high versus low metabolic rates more pronounced and facilitating the direct inference of thermophysiological strategies.	Apart from occasional morphological distortion, diagenesis does not impact the preservation of the bone microstructure used to calculate growth rates.
Species can be analyzed based on a single representative, however, spectral calibration and thermophysiology assessments require a large and diverse sample set.	An ontogenetic series of a given extinct species is required to calculate growth rates (considering that bone resorption increases with age).
Raman assessments of fossil organic matter	*Osteohistological assessments of vascular diameters*[20]
Raman assessments of the relative abundance of metabolic ALEs in modern and fossil amniote bones allow for the direct assessment of metabolic performance and resulting thermoregulatory strategies.	Blood vessel diameters vary within and across skeletal elements. Inferences of metabolic performance from blood vessel diameters as representative of the blood flow required to maintain physiology are indirect and might reflect correlation rather than causation.
Samples require only surface-cleaning with ethanol, and the analysis is fully non-destructive.	Requires destructive sampling and time-intensive preparation (sample cutting, embedding, polishing, etc.).
Diagenesis exacerbates differences in the original relative abundance of ALEs, making the separation of taxa with high versus low metabolic rates more pronounced and facilitating the direct inference of thermophysiological strategies.	Apart from the occasional morphological distortion, diagenesis does not impact the preservation of the bone microstructure used to calculate growth rates.
Species can be analyzed based on a single representative, however, spectral calibration and thermophysiology assessments require a large and diverse sample set.	Comparative assessments of a potential correlation between vascular canal diameter and metabolic rates require a large, extant sample set.
Raman assessments of fossil organic matter	*SEM assessments of fossil blood cell structure and size*[9]
Raman-based metabolic rate assessments are applicable to all amniotes based on the calibration presented here. Future work will likely offer suitable calibrations that allow the integration of other clades into existing data sets.	There are phylogenetic constraints on the size of blood cells, allowing oxygen binding capacity to be inferred based on blood cell size only within comparable clades.

Diagenesis exacerbates differences in the original relative abundance of ALEs, making the separation of taxa with high versus low metabolic rates more pronounced and facilitating the direct inference of thermophysiological strategies.	The effects of diagenesis on blood cell structure and size, particular the resistance to water loss-initiated shrinking during early diagenesis, have not yet been quantified in a phylogenetically diverse sample set.
The approach is non-destructive.	The approach is destructive.

5. References

1. Wiemann, J. et al. Fossilization transforms vertebrate hard tissue proteins into N-heterocyclic polymers. *Nat. Commun.* **9**, 1-9 (2018).
2. Wiemann, J., Crawford, J. M., & Briggs, D. E. G. Phylogenetic and physiological signals in metazoan fossil biomolecules. *Sci. Adv*. **6**, eaba6883 (2020).
3. Wiemann, J., Yang, T.-R. & Norell, M. A. Dinosaur egg colour had a single evolutionary origin. *Nature* **563**, 555-558 (2018).
4. Menges, F. Spectragryph-optical spectroscopy software. *Version*, **1** (2017).
5. Hammer, Ø., Harper, D. A., & Ryan, P. D. PAST: Paleontological statistics software package for education and data analysis. *Palaeontol. Electron.* **4**, 9. (2001).
6. Vistoli, G. et al. Advanced glycoxidation and lipoxidation end products (AGEs and ALEs): an overview of their mechanisms of formation. *Free Radic. Res.* **47**, 3-27 (2013).
7. Pamplona, R. Advanced lipoxidation end-products. *Chem.-Biol. Interact.* **192**, 14-20 (2011).
8. Miyata, T., Kurokawa, K. & Van Ypersele de Strihou, C. Advanced glycation and lipoxidation end products: role of reactive carbonyl compounds generated during carbohydrate and lipid metabolism. *J. Am. Soc. Nephrol.* **11**, 1744-1752 (2000).
9. Plet, C., Grice, K., Pagès, A., Verrall, M., Coolen, M.J., Ruebsam, W., Rickard, W.D. & Schwark, L. Palaeobiology of red and white blood cell-like structures, collagen and cholesterol in an ichthyosaur bone. *Sci. Rep.* **7**, 1-10 (2017).
10. Bennett, A. F. & Nagy, K. A. Energy expenditure in free-ranging lizards. *Ecology* **58**, 697-700 (1977).
11. Pinowski, J. & Kendeigh, S. C. (Eds.). (2012). *Granivorous birds in ecosystems: their evolution, populations, energetics, adaptations, impact and control* (Vol. 12). Cambridge University Press.
12. Taylor, C. R. et al. Design of the mammalian respiratory system. III. Scaling maximum aerobic capacity to body mass: wild and domestic mammals. *Respir. Physiol.* **44**, 25-37 (1981).
13. Koteja, P. On the relation between basal and field metabolic rates in birds and mammals. *Funct. Ecol*. 56-64 (1991).
14. Hinds, D. S. et al. Maximum metabolism and the aerobic factorial scope of endotherms. *J. Exp. Biol.* **182**, 41-56 (1993).
15. Bundle, M. W. et al. High metabolic rates in running birds. *Nature* **397**, 31-32 (1999).
16. McKechnie, A. E. & Wolf, B. O. The allometry of avian basal metabolic rate: good predictions need good data. *Physiol. Biochem. Zool.* **77**, 502-521(2004).
17. Weibel, E. R. et al. Allometric scaling of maximal metabolic rate in mammals: muscle aerobic capacity as determinant factor. *Resp. Physiol. Neurobi.* **140**, 115-132 (2004).
18. Cano, J. M. & Nicieza, A. G. Temperature, metabolic rate, and constraints on locomotor performance in ectotherm vertebrates. *Funct. Ecol.* 464-470 (2006).

19. Worthy, G. A. et al. Basal metabolism of an adult male killer whale (Orcinus orca). *Mar. Mam. Sci.* **30**, 1229-1237 (2013).
20. Legendre, L. J. et al. Palaeohistological evidence for ancestral high metabolic rate in archosaurs. *Syst. Biol.* **65**, 989-996 (2016).
21. Dupoué, A. et al. Climate and foraging mode explain interspecific variation in snake metabolic rates. *P. Royal Soc. B-Biol. Sci.* **284**, 20172108. (2017).
22. Lockyer, C. Body weights of some species of large whales. *ICES J. Mar. Sci.* **36**, 259-273 (1976).
23. Sacher, G. A. Relation of lifespan to brain weight and body weight in mammals. In *Ciba Foundation colloquia on ageing* (Vol. 5, pp. 115-133). Churchill London (1959).
24. Meiri, S. Length–weight allometries in lizards. *J. Zool.* **281**, 218-226 (2010).
25. Benson, R. B. et al. Rates of dinosaur body mass evolution indicate 170 million years of sustained ecological innovation on the avian stem lineage. *PLoS Biol.* **12**, e1001853 (2014).
26. Gillooly, J. F. et al. Body mass scaling of passive oxygen diffusion in endotherms and ectotherms. *Proc. Nat. Acad. Sci.* **113**, 5340-5345 (2016).
27. Grigg, G. C., Beard, L. A. & Augee, M. L. The evolution of endothermy and its diversity in mammals and birds. *Physiol. Biochem. Zool.* **77**, 982-997 (2004).
28. de Ricqles et al. Palaeohistology of the bones of pterosaurs (Reptilia: Archosauria): anatomy, ontogeny, and biomechanical implications. *Zool. Journ. Linn. Soc.* **129**, 349-385 (2000).
29. Rezende, E. L. et al. Shrinking dinosaurs and the evolution of endothermy in birds. *Sci. Adv.* **6**, eaaw4486 (2020).
30. Christian, K. A. & Conley, K. E. Activity and resting metabolism of varanid lizards compared with typical lizards. *Aust. J. Zool.* **42**, 185-193 (1994).
31. Tattersall, G. J. et al. Seasonal reproductive endothermy in tegu lizards. *Sci. Adv.* **2**, e1500951 (2016).
32. Amiot, R. et al. Oxygen isotopes from biogenic apatites suggest widespread endothermy in Cretaceous dinosaurs. *Earth Planet. Sc. Lett.* **246**, 41-54 (2006).
33. Fleischle, C. V., Wintrich, T. & Sander, P. M. Quantitative histological models suggest endothermy in plesiosaurs. *PeerJ* **6**, e4955 (2018).
34. Upham, N. S. et al. Inferring the mammal tree: Species-level sets of phylogenies for questions in ecology, evolution, and conservation. *PLoS Biol.* **17**, e3000494 (2019).
35. Simoes, T. R. et al. The origin of squamates revealed by a Middle Triassic lizard from the Italian Alps. *Nature* **557**, 706-709 (2018).
36. Gauthier, J. A. et al. Assembling the squamate tree of life: perspectives from the phenotype and the fossil record. *Bull. Peabody Mus. Nat.* **53**, 3-308 (2012).
37. Nesbitt, S. J. et al. The earliest bird-line archosaurs and the assembly of the dinosaur body plan. *Nature* **544**, 484-487 (2017).
38. Brusatte, S. L. et al. Gradual assembly of avian body plan culminated in rapid rates of evolution across the dinosaur-bird transition. *Curr. Biol.* **24**, 2386-2392 (2014).
39. Prum, R. O. et al. A comprehensive phylogeny of birds (Aves) using targeted next-generation DNA sequencing. *Nature* **526**, 569-573 (2015).
40. Bapst, D. W. paleotree: an R package for paleontological and phylogenetic analyses of evolution. *Methods Ecol. Evol.* **3**, 803-807 (2012).
41. R Core Team. R: A Language and Environment for Statistical Computing. (2018).
42. Alroy, J. Fossilworks: gateway to the paleobiology database. (2016).
43. Kumar, S., Stecher, G., Suleski, M. & Hedges, S. B. TimeTree: a resource for timelines, timetrees, and divergence times. Mol. Biol. Evol. 34, 1812–1819 (2017).

44. Revell, L. J. phytools: An R package for phylogenetic comparative biology (and other things). *Methods Ecol. Evol.* **3**, 217-223 (2012).
45. Baudinette, R. V. Scaling of heart rate during locomotion in mammals. *J. Comp. Physiol.* **127**, 337-342 (1978).
46. Taylor, C. R. et al. Energetics and mechanics of terrestrial locomotion. I. Metabolic energy consumption as a function of speed and body size in birds and mammals. *J. Exp. Biol.* **97**, 1-21 (1982).
47. Heglund, N. C. et al. Energetics and mechanics of terrestrial locomotion. IV. Total mechanical energy changes as a function of speed and body size in birds and mammals. *J. Exp. Biol.* **97**, 57-66 (1982).
48. Garland, T. The relation between maximal running speed and body mass in terrestrial mammals. *J. Zool.* **199**, 157-170 (1983).
49. Karasov, W. H. Daily energy expenditure and the cost of activity in mammals. *Am. Zool.* **32**, 238-248 (1992).
50. Berner, R.A. GEOCARBSULF: a combined model for Phanerozoic atmospheric O_2 and CO_2. *Geochim. Cosmochim. Ac.* **70**, 5653-5664 (2006).
51. Padian, K. & Lamm, E. T. (Eds.). (2013). *Bone histology of fossil tetrapods: advancing methods, analysis, and interpretation*. Univ of California Press.
52. Erickson, G. M. et al. Dinosaurian growth patterns and rapid avian growth rates. *Nature* **412**, 429-433 (2001).
53. Ibrahim, N. et al. Semiaquatic adaptations in a giant predatory dinosaur. *Science* **345**, 1613-1616 (2014).
54. O'Connor, J. et al. Medullary bone in an Early Cretaceous enantiornithine bird and discussion regarding its identification in fossils. *Nat. Commun.* **9**, 1-8 (2018).
55. Lee, A. H. & Werning, S. Sexual maturity in growing dinosaurs does not fit reptilian growth models. *Proc. Nat. Acad. Sci.* **105**, 582-587 (2008).
56. Erickson, G. M. et al. Tyrannosaur life tables: an example of nonavian dinosaur population biology. *Science* **313**, 213-217 (2006).
57. Woodward, H. N. et al. Maiasaura, a model organism for extinct vertebrate population biology: a large sample statistical assessment of growth dynamics and survivorship. *Paleobiology* **41**, 503-527 (2015).
58. Erickson, G. M. et al. Gigantism and comparative life-history parameters of tyrannosaurid dinosaurs. *Nature* **430**, 772-775 (2004).
59. Erickson, G. M. et al. Dinosaur incubation periods directly determined from growth-line counts in embryonic teeth show reptilian-grade development. *Proc. Nat. Acad. Sci.* **114**, 540-545 (2017).
60. Padian, K. et al. Dinosaurian growth rates and bird origins. *Nature* **412**, 405 (2001).
61. Horner, J. R. et al. Long bone histology of the hadrosaurid dinosaur Maiasaura peeblesorum: growth dynamics and physiology based on an ontogenetic series of skeletal elements. *J. Vertebr. Paleontol.* **20**, 115-129 (2000).
62. Cubo, J. et al. Paleohistological estimation of bone growth rate in extinct archosaurs. *Paleobiology* **38**, 335-349 (2012).
63. de Margerie, E. et al. Bone typology and growth rate: testing and quantifying 'Amprino's rule' in the mallard (Anas platyrhynchos). *C. R. Biol.* **325**, 221-230 (2002).
64. Grady, J. M. et al. Evidence for mesothermy in dinosaurs. *Science* **344**, 1268-1272 (2014).
65. D'Emic, M. D. Comment on "Evidence for mesothermy in dinosaurs". *Science* **348**, 982-982 (2015).

66. Myhrvold, N. P. Dinosaur metabolism and the allometry of maximum growth rate. *PloS one* **11** (2016).
67. Klevezal, G. A. Reconstruction of individual life histories of rodents from their teeth and bone. *Acta Theriol*. **47**, 127 (1996).
68. Bernard, A. et al. Regulation of body temperature by some Mesozoic marine reptiles. *Science* **328**, 1379-1382 (2010).
69. Eagle, R. A. et al. Dinosaur body temperatures determined from isotopic (13C-18O) ordering in fossil biominerals. *Science* **333**, 443-445 (2011).
70. Eagle, R. A. et al. Isotopic ordering in eggshells reflects body temperatures and suggests differing thermophysiology in two Cretaceous dinosaurs. *Nat. Commun.* **6**, 1-11 (2015).
71. Fricke, H. C. & Rogers, R. R. Multiple taxon–multiple locality approach to providing oxygen isotope evidence for warm-blooded theropod dinosaurs. *Geology* **28**, 799-802 (2000).
72. Dawson, R.R., Field, D.J., Hull, P.M., Zelenitsky, D.K., Therrien, F. and Affek, H.P. Eggshell geochemistry reveals ancestral metabolic thermoregulation in Dinosauria. *Sci. Adv.* **6**, eaax9361 (2020).